

Electroosmosis-Driven Hydrogel Actuators Using Hydrophobic/Hydrophilic Layer-By-Layer Assembly-Induced Crack Electrodes

Jongkuk Ko, Dongjin Kim, Yongkwon Song, Seokmin Lee, Minseong Kwon, Seungyong Han, Daeshik Kang, Yongju Kim, June Huh, Je-Sung Koh,* and Jinhan Cho*

Cite This: *ACS Nano* 2020, 14, 11906–11918

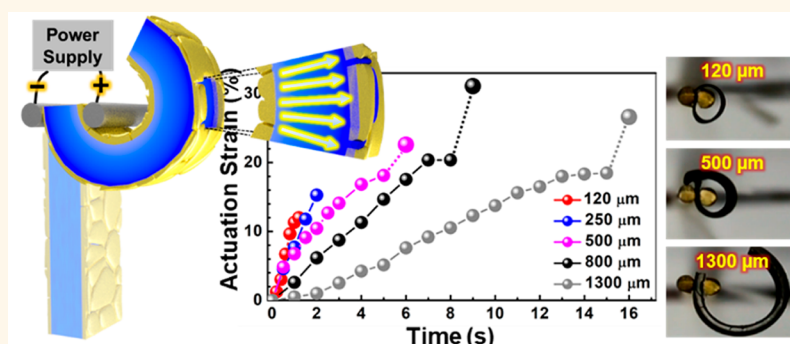
Read Online

ACCESS |

Metrics & More

Article Recommendations

Supporting Information



ABSTRACT: Development of soft actuators with higher performance and more versatile controllability has been strongly required for further innovative advancement of various soft applications. Among various soft actuators, electrochemical actuators have attracted much attention due to their lightweight, simple device configuration, and facile low-voltage control. However, the reported performances have not been satisfactory because their working mechanism depends on the limited electrode expansion by conventional electrochemical reactions. Herein, we report an electroosmosis-driven hydrogel actuator with a fully soft monolithic structure-based whole-body actuation mechanism using an amphiphilic interaction-induced layer-by-layer assembly. For this study, cracked electrodes with interconnected metal nanoparticles are prepared on hydrogels through layer-by-layer assembly and shape transformation of metal nanoparticles at hydrophobic/hydrophilic solvent interfaces. Electroosmotic pumping by cracked electrodes instantaneously induces hydrogel swelling through reversible and substantial hydraulic flow. The resultant actuator exhibits actuation strain of higher than 20% and energy density of $1.06 \times 10^5 \text{ J m}^{-3}$, allowing various geometries (e.g., curved-planar and square-pillared structures) and motions (e.g., slow-relaxation, spring-out, and two degree of freedom bending). In particular, the energy density of our actuators shows about 10-fold improvement than those of skeletal muscle, electrochemical actuators, and various stimuli-responsive hydrogel actuators reported to date.

KEYWORDS: electroosmosis-driven hydrogel actuator, crack electrode, metal nanoparticle, hydrophobic/hydrophilic layer-by-layer assembly, swelling/deswelling

Electrochemical actuators with one degree of freedom (1-DOF) of movement based on changes in electrode volume have attracted much attention in the area of soft actuators due to their lightweight, facile electrical control, and relatively low power consumption compared to other types of soft actuators.^{1–15} Although a substantial amount of research has focused on enhancing the performance (particularly the actuation strain, energy density, and DOFs) of electrochemical actuators, their performance is considerably restricted by the relatively small volume change in electrodes via conventional

electrochemical reaction-based mechanisms (i.e., electric double layer (EDL) capacitive and/or pseudocapacitive reactions) as

Received: June 12, 2020
Accepted: September 4, 2020
Published: September 4, 2020



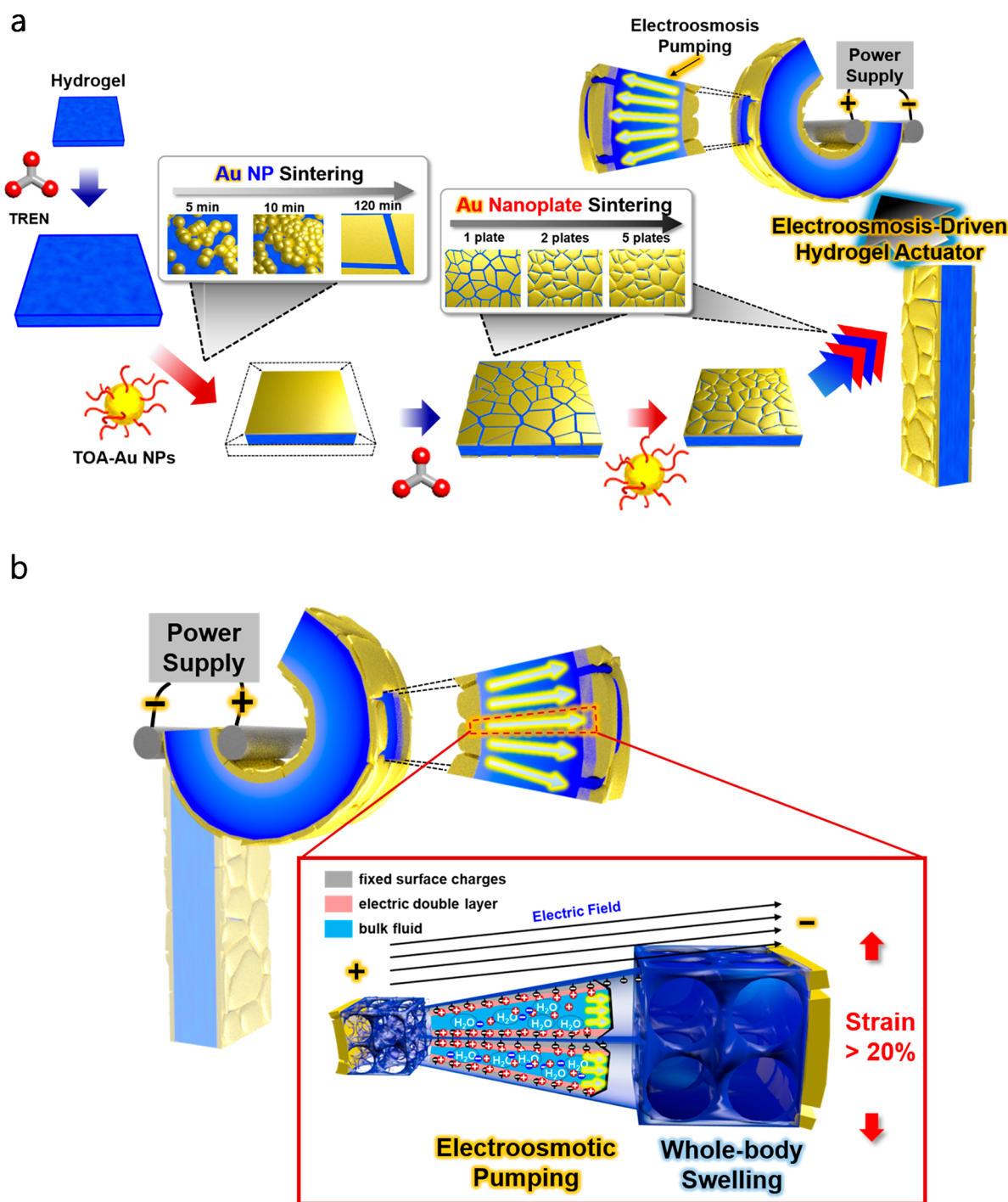


Figure 1. (a) Schematic illustration of the formation of cracked electrode with interconnection prepared from interfacial assembly and room-temperature sintering of TOA-Au NPs on hydrogel for EOP hydrogel actuator. (b) Schematic illustration showing the working mechanism of EOP hydrogel actuator using LbL assembly induced cracked electrodes.

well as the low electrical conductivities of electrode materials (i.e., carbon materials and conductive polymers).^{1–12} In most cases, these actuators exhibit one-dimensional bending with less than 2% strain.^{3–12}

As another type of soft actuator, hydrogel actuator has also been widely studied. Their working mechanisms are mainly based on the distinctive properties of hydrogels that can have a large degree of swelling-induced volume changes according to various environmental stimuli such as heat,^{16,17} light,^{18,19} chemical,^{20,21} and/or pH²² without additional deposition of

electrically conductive electrodes onto hydrogels. However, these actuators have exhibited slow actuation and low Young's modulus of hydrogels, resulting in limited controllability and low energy/power density. Although the bilayer-structured actuators based on humidity-responsive layers^{23–25} have exhibited enhanced performance of high actuation strain with fast response time, the humidity variation for actuation and the limited thickness of actuator have restricted their wide applications. Considering that the above-mentioned drawbacks of conventional soft actuators are mainly based on the limit of

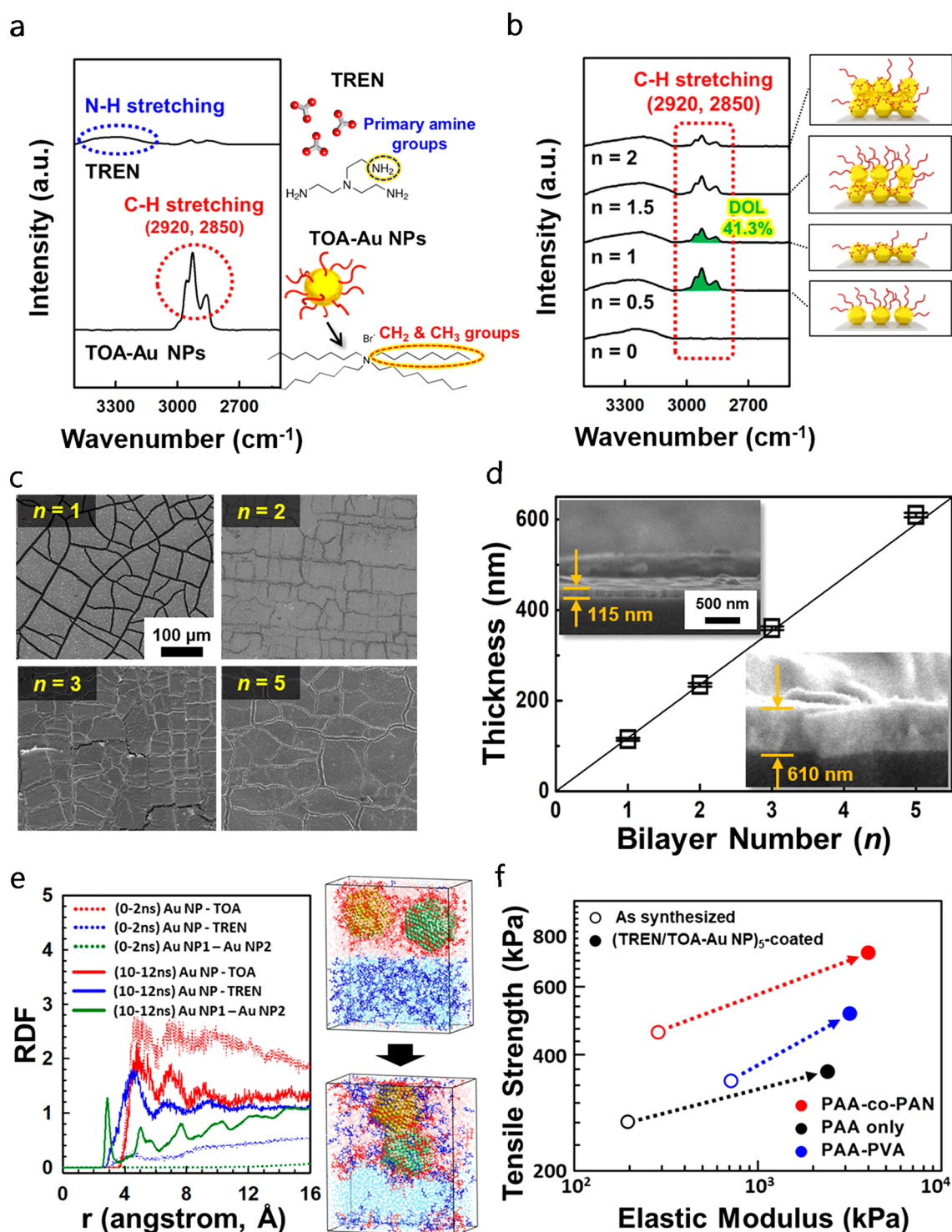


Figure 2. (a) FTIR spectra of TREN with three primary amino groups and TOA-Au NPs. (b) FTIR spectra of (TREN/TOA-Au NP)_n multilayers showing the TREN N-H stretching band (3300–3500 cm⁻¹) and the TOA ligand displays C-H stretching peaks corresponding to the long alkyl chains at 2850 and 2920 cm⁻¹. A degree of the ligand exchange (DOL) reaction was calculated by comparing the integral of the TOA absorbance peak with that of long alkyl chains at 2850–2920 cm⁻¹ before and after the adsorption of TREN onto the TOA-Au NP layer. It was calculated that 41.3% of TOA ligands bound to the surface of Au NPs were replaced with TREN in an aqueous state. (c) Planar FE-SEM images of (TREN/TOA-Au NP)_n/TREN multilayer-coated hydrogels. (d) Thicknesses of (TREN/TOA-Au NP)_n multilayers deposited on hydrogels with increasing bilayer number (*n*) from 1 to 5. The inset shows the cross-section FE-SEM images of multilayer-coated hydrogels. (e) Radial distribution functions of the center-of-mass of TOA (red), TREN (blue) around Au NP, and that between two different Au NPs (denoted AuNP1 and AuNP2, green) in the simulation time span of 0–2 ns (dotted lines) and 10–12 ns (solid lines). Images on the right represent snapshots of the MD-simulated model structures at 10² ps (top) and at 10⁴ ps (bottom). In the snapshots, the system constituents are shown in different colors for visual clarity: AuNP1 (yellow), AuNP2 (light green), TOA (red), TREN (blue), toluene (translucent red), and water (translucent blue). (f) Tensile strength and Young's modulus of as-synthesized and (TREN/TOA-Au NP)₅-coated PAA-co-PAN, PAA only, and PAA-PVA hydrogels.

their intrinsic working mechanism, the realization of unusual mechanism-based soft actuator that can be actuated with large actuation strain, multi-DOF controllability, and high energy/power density in response to external stimuli are strongly required for the development of various next-generation soft systems, including soft robots, artificial skins, and intelligent sensors.

As another working mechanism for possibly operating an electroactive actuator, an electrokinetic pumping mechanism can generate bulk fluid flow by electric fields which has been generally based on bulky and rigid pumping systems over the past several decades.^{26–30} Although these pumping systems have had much difficulty in being directly applied to the soft actuators due to their rigid frame structure, Cacucciolo and co-workers have recently reported an elastomer-based pump that can be operated by the charge-injection electro-hydrodynamics of a dielectric liquid.³¹ They have also demonstrated that the developed soft pumps are flexible, stretchable, and are even applicable for soft actuators. However, despite the use of the electrokinetic pumping system, it still suffers from high voltage operation (\sim kV), slow actuation, and limited actuation dimension (1D) for the application of soft actuators. In this regard, developing a high-performance soft actuator with low operation voltage and fast actuation can provide a basis for a major breakthrough in the field of various soft actuators.

Here, we report an electroosmotic pump-driven (EOP) hydrogel actuator with a low operating voltage, fast actuation, monolithic structure-based whole-body actuation mechanism, and multi-DOF movement that is operated by massive fluid flow-induced hydrogel swelling through electroosmosis pumping (Figure 1a). Although an ion electroosmosis-based osmotic actuator³² among previously reported osmotic flow-driven actuators^{33–35} has demonstrated the low-voltage operation and the possibility for miniaturization, it still suffers from the limited movement and the slow actuation. We highlight that our EOP hydrogel actuator is, in view of the working mechanism, electrode materials, and structure design, basically different from the previously reported electrochemical actuators, hydrogel actuators, and osmotic flow driven actuators.

To prepare this actuator, metal nanoparticles (NPs) in nonpolar media were first layer-by-layer (LbL)-assembled onto a hydrogel using small-molecule linkers in water, which generated cracked electrodes composed of highly interconnected metal NPs. That is, all the components required for the electrokinetic pump (specifically electroosmosis pump) are embedded onto the hydrogel. In particular, we highlight that cracked electrodes with mechanically compliant properties and high electrical conductivity are prepared through the *in situ* cooperation of interfacial LbL assembly and room-temperature sintering of metal NPs on hydrogels without the need for additional treatment processes. This approach is in stark contrast to typical cracked electrodes that are formed by chemical reduction, sputtering, or spin-casting with subsequent mechanical stretching.^{36–39} In most cases, the previously reported cracked electrodes exhibited a drastic decrease in electrical conductivity at relatively low strain ($<2\%$ strain).^{36,37} Although it was reported that some cracked electrodes with a percolation network could maintain electrical conductivity over 20% strain ($>100 \Omega \text{ sq}^{-1}$ at 20% strain), the previous approaches could be restrictively applied to dried elastomers with flat structures.^{38,39} However, the cracked electrodes with a high level of interconnection through LbL assembly are covalently bonded to the hydrogel, which can preserve their high electrical

conductivity and robust structure even under large mechanical deformation.

Another notable benefit of our actuator is that an acrylic, acid-based hydrogel serves as a porous membrane and an ionic liquid reservoir for electroosmosis as well as an actuation body for swelling. Specifically, when the operating voltage of approximately 3 V was applied to the cracked electrodes, reversible and substantial hydraulic fluid flow was generated rapidly, which induced hydrogel swelling (Figure 1b). These phenomena imply that our EOP hydrogel actuators are dominantly actuated by whole-body (hydrogel) swelling by the reversible bulk fluid of a hydrated ionic liquid, which is evidently different from electrochemical actuators with electrode expansion by electrochemical reactions as well as typical electroosmosis devices with bulky and rigid system (Figures S1 and S2). Because of the distinctive operation mechanism and electrode structure, these EOP actuators exhibited high actuation performances (i.e., an actuation strain of 23% , an energy density of $1.06 \times 10^5 \text{ J m}^{-3}$, and a power consumption/strain of $4 \text{ mW cm}^{-2} \%^{-1}$) and allowed 2-DOF movement, outperforming a variety of different kinds of hydrogel actuators,^{16–22} other osmosis-based actuators^{33–35} as well as electrochemical actuators (actuation strain $<2\%$, energy density $<1.2 \times 10^4 \text{ J m}^{-3}$ and power consumption/strain of $40 \text{ mW cm}^{-2} \%^{-1}$)^{6,8} reported to date. Particularly, it is noteworthy that our actuators exhibited about 10-fold enhancement in energy density compared with those of mammalian skeletal muscle ($<8.1 \times 10^3 \text{ J m}^{-3}$),⁴⁰ electrochemical actuators ($<1.2 \times 10^4 \text{ J m}^{-3}$),^{6,8} and various-stimuli responsive hydrogel actuators ($<10^4 \text{ J m}^{-3}$).¹⁶ We believe that our approach can provide a basis for further advance in soft actuators.

RESULTS AND DISCUSSION

Fabrication of Cracked Electrode with Interconnection on Hydrogel. First, hydrophobic tetraoctylammonium (TOA)-stabilized Au NPs (TOA-Au NPs) with a diameter of 8 nm in a nonpolar medium (toluene) were consecutively LbL assembled with tris(2-aminoethyl)amine (TREN) in water onto poly(acrylic acid) (PAA)-based hydrogels using a ligand exchange reaction between the bulky TOA ligands and TREN linkers (Figures S3 and S4). This reaction was confirmed by Fourier transform infrared (FTIR) spectroscopy (Figure 2a,b). The consecutive replacement of bulky TOA ligands by TREN molecular linkers to overcome the extremely different solvent polarities between nonpolar and aqueous media can significantly decrease the separation distance (i.e., contact resistance) between neighboring Au NPs in the vertical dimension. The minimized interparticle distance induced partial sintering of densely packed Au NPs at room temperature without additional chemical and/or physical treatment. This also caused the spread of sintered Au NPs in the lateral and vertical dimensions with an increasing adsorption time of the NPs (Figure S5). The hydrogel film was subjected to repetitive swelling (for the deposition of TREN in water) and deswelling (for the deposition of TOA-Au NPs in toluene) during LbL assembly in aqueous and nonpolar media, respectively. This amphiphilic assembly generated a few notable features. Specifically, if the swollen TREN-coated hydrogel was immersed in a toluene solution of TOA-Au NPs, the NPs were covalently adsorbed onto the TREN-coated hydrogels through ligand exchange; simultaneously, the hydrogel contracted in toluene (Figure 2c and Figure S6). During the deswelling–LbL assembly process, the TOA-Au NPs were continuously adsorbed onto the wet surface of the soft hydrogel film that contained a large amount of residual aqueous TREN

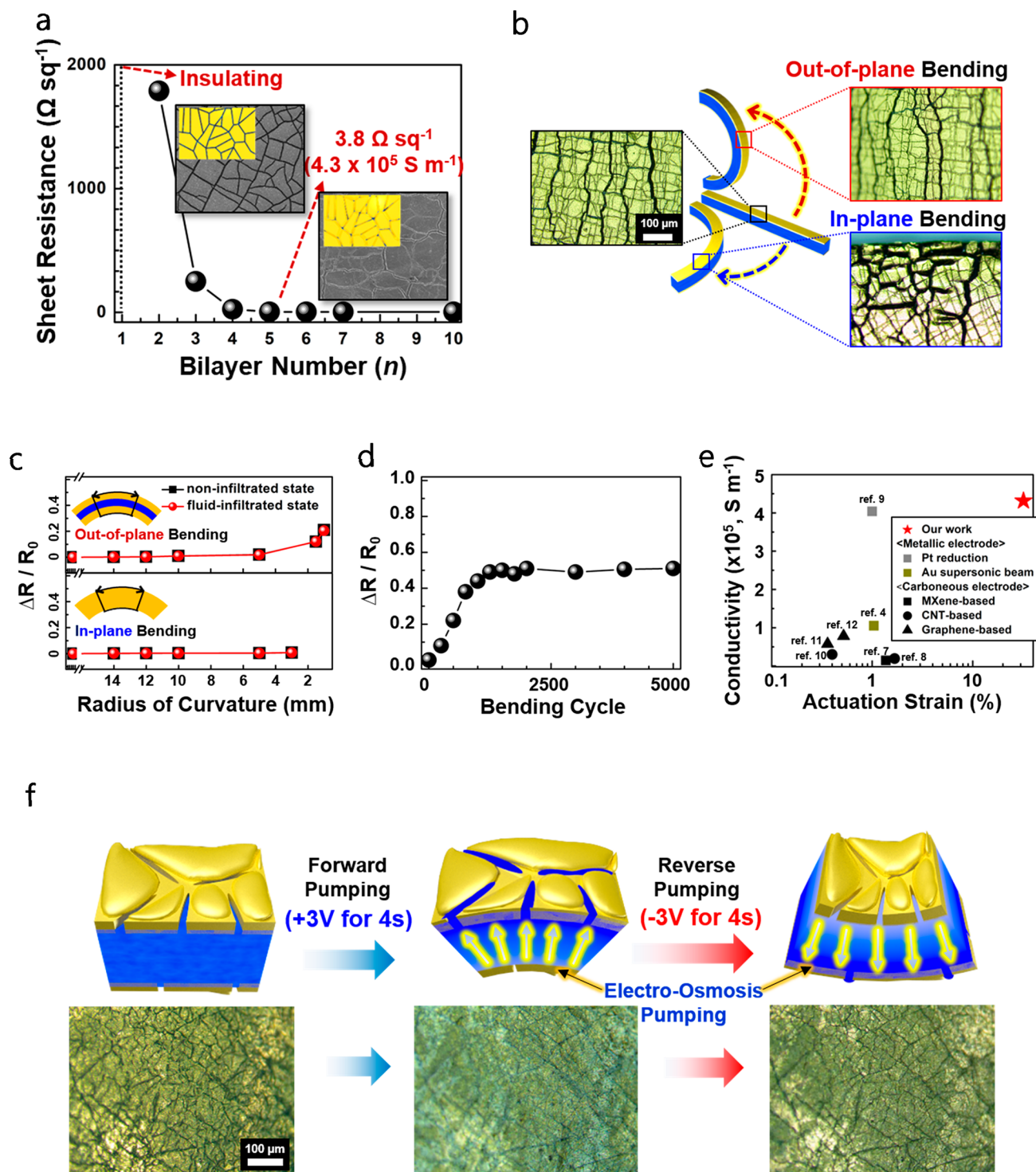


Figure 3. (a) Sheet resistance of the cracked electrode with interconnection coated on PAA-co-PAN hydrogel as a function of bilayer number (n). (b) Illustration and optical images of $[\text{Au NP}]_5$ -coated hydrogels in the neutral state, out-of-plane bending direction, and in-plane bending direction. (c) Resistance changes of $[\text{Au NP}]_5$ -coated PAA-co-PAN hydrogels with ionic-fluid-infiltrated and noninfiltrated states as a function of the bending radius in the out-of-plane and in-plane directions. (d) Electrical stability of $[\text{Au NP}]_5$ -coated PAA-co-PAN hydrogel as a function of bending cycle number. (e) Plots of electrical conductivity versus actuation strain of the $[\text{Au NP}]_5$ -coated hydrogel electrode for EOP actuator and the previously reported carbon material- and metal-coated electrodes for electrochemical actuators. (f) Illustration and optical images showing reversible electroosmosis pumping by forward and reverse bias on $[\text{Au NP}]_5$ -coated PAA-co-PAN.

solution, which effectively converted from partially sintered Au NPs to Au nanoplates with nanoscale thickness. These phenomena are similar to those of time- and concentration-dependent interfacial NP assembly occurring at the interface between two immiscible solutions (Figure S7). Therefore, upon

increasing the bilayer number (n) of $(\text{TOA-Au NP}/\text{TREN})_n$ multilayers from 1 to 5, the thickness of the Au nanoplates almost linearly increased from 115 to 610 nm, resulting in a relatively thick Au NP nanoplate (average thickness $\sim 117 \pm 3$ nm) per bilayer (Figure 2d). It should also be noted that our

approach inducing metallic sintering and shape transformation can significantly enhance the electrical conductivity of Au NP-based multilayers due to their increased connectivity, which in terms of adsorption behavior is different from the typical interfacial assembly⁴¹ and the reported LbL assemblies^{42–45} with insufficient lateral surface coverage per layer in organic/organic or aqueous/aqueous media.

The structural evolution of initially unsintered NPs during ligand exchange was further confirmed by atomistic molecular dynamics (MD) based on a minimal system composed of two TOA-Au NPs (in toluene) interfaced with TREN (in water) (Figure 2e and Movie 1). The radial distribution functions (RDFs) of the center of mass (COM) of the organic species (TOA ligands and TREN linkers) around the Au NPs were computed from the MD trajectories (Figure 2e). The first RDF peak for TREN increased as that for TOA decreased, indicating the spontaneous exchange of TOA with TREN. The shorter the distance between the Au NP and the first neighboring TREN linker (corresponding to the first RDF peak for TREN) is, the less steric repulsion there should be between the substituted TREN linkers and the Au NP and, thus, a greater chance for NP sintering to occur. Consequently, the RDF between two different Au NPs shows a pronounced peak at the radial distance corresponding to the shortest interatomic spacing (2.884 Å) for the Au crystal; this result indicates that the two Au NPs are sintered, as also demonstrated by the simulated structure. Therefore, these simulation results show that the deposition of hydrophobic Au NPs in toluene onto the wet surface of TREN-coated hydrogel films can induce metallic sintering via ligand exchange reactions.

Another notable feature of our approach is that the repetitive swelling–deswelling process, which occurs during metallic sintering between newly adsorbed Au NPs and preadsorbed Au nanoplates as well as between neighboring Au NPs, effectively generates highly interconnected cracks with large domains and cracks ranging in size from a few to tens of micrometers. That is, when the TOA-Au NP-coated hydrogel is immersed in an aqueous TREN solution, the formed Au NP nanoplates are segmentally cracked in the reswollen hydrogel. In this case, the LbL-assembled hydrogels repeatedly undergo swelling and deswelling with an approximate volume change of 30% during LbL deposition (Figure S6). This adsorption, together with the residual stress resulting from the assembly of Au nanoplates in the lateral dimension, induces the isotropically cracked structure. However, the continuous LbL deposition led to a solder-like interconnection between vertically adjacent crack domains through multiple cracked nanoplates (see Figure 2c and Figure S8). It should also be noted that the structure of crack electrodes could be further modulated by LbL assembly conditions. That is, the size of crack or the formation of anisotropic cracks could be controlled by changing the deposition time of TOA-Au NPs or by applying the prestrain on the (TOA-Au NP/TREN)_n multilayer-coated hydrogels, respectively (Figure S9). Furthermore, our approach can be easily applied to hydrogels with various shapes (Figure S10).

The mechanical properties of hydrogel-based actuators are also important factors for high-energy density actuation performance. When the hydrogels were immersed in a TREN solution (pH 11), the COOH groups of the PAA-based hydrogels [i.e., PAA, blended poly(acrylic acid)-poly(vinyl alcohol) (PAA-PVA), and poly(acrylic acid)-*co*-poly(acrylonitrile) (PAA-*co*-PAN)] were converted to the carboxylated ion (COO[−]) groups. The strong electrostatic repulsion

between the COO[−] groups caused the hydrogels to significantly swell (more than 8-fold in volume), and the adsorbed TREN linkers resulted in the formation of hydrogen bonds and/or electrostatic interaction-induced cross-links between the NH₂/NH₃⁺ groups of TREN and the COO[−]/COOH groups of the hydrogels. Furthermore, the subsequent deposition of hydrophobic TOA-Au NPs in toluene onto the outermost TREN layer increased the mechanical properties of the hydrogel accompanying the deswelling phenomenon (Figure S11). Specifically, in the case of the PAA-*co*-PAN hydrogel the Young's modulus of (TREN/TOA-Au NP)₅-coated hydrogels notably increased from 700 kPa to 4 MPa as the bilayer number (*n*) increased from 0 to 5 (Figure 2f). Additionally, PAA-*co*-PAN hydrogel showed the highly porous structures with the pore size of 2–7 μm (Figure S12).

Electrical Properties of Cracked Electrodes. We investigated the electrical properties of the (TREN/TOA-Au NP)_n-coated PAA-*co*-PAN hydrogel (hereafter abbreviated as “[Au NP]_n-hydrogel”) (Figure 3a and Figure S13). First, the cracked electrodes formed from the deposition of (TREN/TOA-Au NP)_n (where *n* = 1 or 2) on the hydrogel exhibited relatively high sheet resistance (>1700 Ω sq^{−1}). However, as the bilayer number (*n*) of (TREN/TOA-Au NP)_n (or the number of Au nanoplates) was increased from 2 to 10, the sheet resistance of the [Au NP]_n-hydrogel electrode significantly decreased to approximately 3.8 Ω sq^{−1} (an electrical conductivity of 4.3 × 10⁵ S m^{−1}) reaching a plateau at *n* = 5, which was also observed for other PAA-based hydrogel electrodes (Figure 3a and Figure S13). In addition, electrical resistances of crack electrodes strongly depended on the bilayer number (*n*) of (TREN/TOA-Au NP)_n-coated PAA-*co*-PAN hydrogels as well as the radius of bending curvature (Figure S14). This phenomenon was mainly caused by both the increased interconnection of cracked Au nanoplates and the partial metallic sintering as the bilayer number was increased. In particular, the cracked electrodes with interconnection by multistacked nanoplates exhibited high electrical stability even under in-plane and out-of-plane bending modes, as expected from the optical images of the electrodes maintaining their interconnections under deformation (Figure 3b). Although the bending radius for the in-plane and out-of-plane bending tests decreased up to 1 and 3 mm, respectively, the sheet resistances of the bent electrodes were kept below 3.9 and 5.0 Ω sq^{−1}, respectively (Figure 3c). We also confirmed that the sheet resistance was maintained at less than 10 Ω sq^{−1} during a repetitive bending test over at least 5000 cycles (Figure 3d). Moreover, as shown in Figure S15, the (TREN/TOA-Au NP)₅ multilayers were tightly bonded on PAA-*co*-PAN hydrogels (i.e., by covalent bonding) even after repetitive mechanical bending tests of 1000 cycles and after actuation at 3 V. Given that previously reported metal-deposited hydrogel electrodes prepared using a chemical reduction method could maintain their electrical conductivity only under the restricted bending conditions of strain and direction,^{13,14} our results suggest that these cracked electrodes can be directly applied in actuators, allowing high actuation strain. Additionally, these high and stable electrical conductivities of [Au NP]_n-hydrogel electrode outperformed those of previously reported carbon material or metal (mainly by chemical reduction of metal ions)-based electrodes (Figure 3e).

On the basis of the high electrical and mechanical stabilities of cracked electrodes, we prepared an electroosmosis-driven hydrogel actuator with a monolithic structure. Generally, electroosmosis drives the bulk-fluid flow by applying a tangential

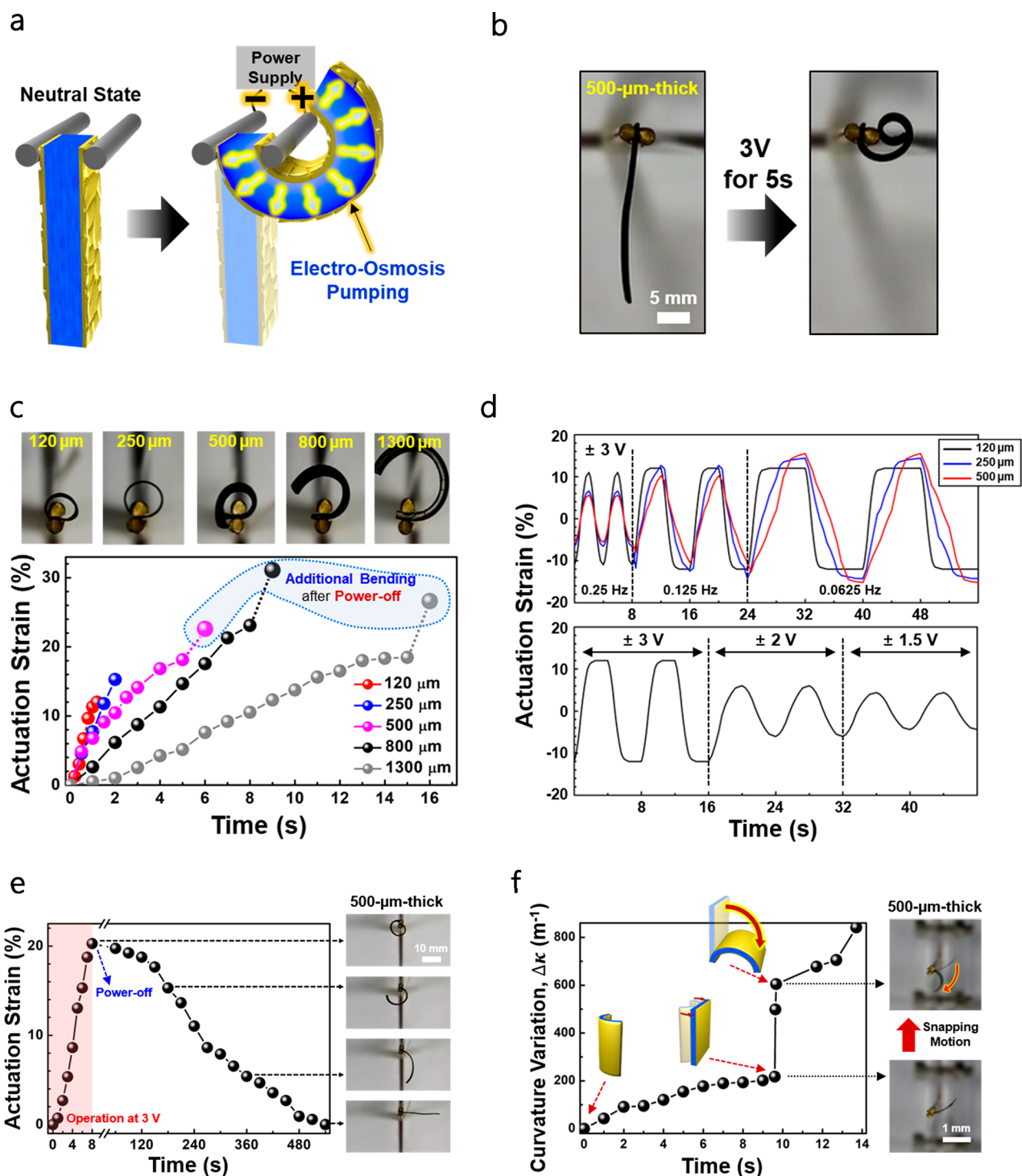


Figure 4. (a) Schematic illustration of the EOP actuator operating from electroosmosis pumping. (b) Photographic images of 500 μm thick EOP actuator (i.e., $[\text{Au NP}]_5$ -coated PAA-co-PAN) operating at 3 V. (c) Time-dependent actuation strain of EOP actuators with hydrogels of different thickness. In this case, EOP actuators were operated at 3 V. (d) Time-dependent actuation strain of EOP actuators as a function of total thickness and AC voltage. (e) Time-dependent actuation strain of the 500 μm thick EOP actuator showing slow-relaxation property measured at a voltage of 3 V. (f) Time-dependent curvature variation of the 500 μm thick EOP actuator with a bistable geometry measured at a voltage of 3 V.

electric field on a microchannel in the presence of an EDL (see Figure S1). In contrast to conventional electroosmotic devices based on rigid and bulky components, our electroosmotic actuator is characterized by the facts that all the required components are integrated on acrylic acid-based hydrogels, and the hydrogel itself serves as a porous membrane and an ionic liquid reservoir for electroosmosis. Furthermore, considering

that our actuator can minimize the distance between the electrode and membrane, operation voltages can be significantly reduced.^{28–30}

For actuator operation, $[\text{Au NP}]_5$ -hydrogels were first immersed in a 1:1 mixture of aqueous TREN solution and 1-ethyl-3-methylimidazolium tetrafluoroborate ($[\text{EMIM}][\text{BF}_4]$) so that the hydrated ionic fluid could easily infiltrate into the

acrylic acid-based hydrogels. In this case, EDLs were formed on the surfaces of microporous hydrogels that were in contact with a hydrated ionic liquid. When an operation voltage of 3 V was applied to the 1 mm thick [Au NP]₅-hydrogel electrode, the hydrated ionic fluid was rapidly pumped out of the hydrogels through the microcracked region (Figure 3f and Movie S2) due to the interaction of EDLs with the electric field, which consequently dragged the bulk fluid. This low operating voltage made a striking contrast to several thousand operating voltages required for flat metal electrode-based pump systems reported by other research groups.^{26,27,31} Additionally, these phenomena could be reversibly repeated according to the applied forward and reverse operating voltage without notable changes of crack structures on electrodes. Specifically, when operated at 2 V this electroosmosis pumping could be repeated for more than 500 cycles (Figure S16).

Performance of EOP Actuators. Encouraged by the notable electrical, mechanical, and electroosmotic pump properties of cracked-electrode-coated hydrogels, we investigated the actuation performance of electroosmotic pump hydrogel actuators (i.e., EOP actuators) (Figure 4a). Pt-coated poles with a diameter of 2 mm were used as external supports for preventing the damage of electrodes during actuation (Figure S17). First, EOP actuators with planar structures (0.5 cm × 2.5 cm × 500 μm) composed of three types of PAA-based hydrogels exhibited a high bending performance of >20% actuation strain with an operating voltage of 3 V applied for 6 s (Figure 4b and Figure S18). Particularly, the PAA-co-PAN-based EOP actuator displayed a slightly higher actuation performance than the others, and thus was chosen as a model system for an EOP actuator.

We further examined the actuation strain of the EOP actuators (specifically, [Au NP]₅-PAA-co-PAN) with different thicknesses from 120 to 1300 μm as a function of operating time at 3 V (Figure 4c and Movie S3). Although the performance of conventional electrochemical actuators rapidly deteriorated with increasing total thickness,^{7,15} all the samples shown in our study displayed high bending strain with low power consumption (<100 mW cm⁻²). A high actuation strain of 23% was obtained in the 800 μm thick EOP actuator. In particular, actuation could be increased up to over 30% by the aid of the overpumped fluid that induced additional hydrogel swelling after the power was turned off (Figure 4c). Although the maximum available actuation performance of 120 and 250 μm thick EOP actuators could not be achieved at ±3 V owing to the limited bending radius by the copper poles used in our system (Figure S19), they could be operated at AC voltage of 3 V, displaying the actuation strain of above 10% (Figure 4d). The 120 μm thick EOP actuator exhibited high bending strain of 6% and 4.2% at AC voltages of 2 and 1.5 V, respectively (Figure 4d). EOP actuators could also be operated at a considerably low operating voltage of 0.5 V, and additionally exhibit relatively high bending strain of above 1% under extremely low power consumption of 2 mW cm⁻² (Figure S20). By repetitively soaking the actuators in electrolyte solutions for 10–20 s per every 100 cycles, the EOP actuators could be operated during more than 1000 cycles, which maintained approximately 97% of their initial performance (Figure S21). It should also be noted that the EOP actuators operated at 3 V exhibited the blocking force of 19 mN (Figure S22) and the weight-lifting ratio of approximately 30 (Figure S23), which was higher than those of previously reported electrochemical actuators^{8,46} measured at

similar conditions (specifically, blocking force of 115 μm thick sample at 2.5 V ~ 6 mN⁸ and weight-lifting ratio of 20⁴⁶).

Another notable feature of EOP hydrogel actuators is that they can readily realize slow-relaxation and spring-out modes as well as the above-mentioned bending mode without any complex treatment or process.⁴⁷ Specifically, EOP actuators maintained their bent state for a period without additional input energy after the power was turned off (i.e., slow-relaxation) because the confined fluid in and around the electrodes after pumping slowly reverted to its unrestricted state (or equilibrium state). In the case of the 500 μm thick EOP actuator, several minutes were required for its slow-relaxation to be completely released into the equilibrium state, which would be beneficial for soft grippers (Figure 4e). Moreover, the spring-out mode, characterized by a sudden increase in bending motion, was observed by the instantaneous release of accumulated energy in the bent structures of EOP actuators, which was similar to the motion mode of a Venus flytrap with a bistable geometric structure. The artificial Venus flytrap leaf (AVFL) has attracted extensive attention in that it can take advantage of fast snapping motion of a natural Venus flytrap. However, the previously reported approaches have much difficulty in fabricating the high-performance electroactive AVFL. Specifically, an electroactive AVFL system has been realized through ionic polymer metal composite (IPMC)⁴⁸ with simple bending motion or the shape memory alloys (SMA),⁴⁹ which inevitably generated bulky and complicated actuating systems. However, it should be noted that our EOP actuator could easily realize the snapping motion of a Venus flytrap by using its own bistable body structure, which was very similar to the working mechanism of environmental-stimuli responsive AVFL systems^{25,50} as well as a natural *Venus flytrap*. When an operating voltage of 3 V was continuously applied to the 500 μm-thick EOP actuator, its snapping motion showed the fast characteristic time of about 0.1 s compared to normal bending of planar EOP actuator (~5 s) (Figure 4f and Movie S4). Although it took approximately 10 s to accumulate the energy in the bistable structure for rapid movement, this instantaneous movement of EOP actuator was very similar to that of snap-through movement by the Venus flytrap.

To further demonstrate the superiority of EOP actuators, the actuation strain, energy density (ρ_E), and power density (ρ_W) of EOP actuators were compared with the previously reported results (the details are given in Experimental Section). Since hydrogel actuators and electrochemical actuators contained different amounts of water or solvent in their bodies, the energy densities and power densities of various actuators were obtained using a unit-volume basis for quantitative comparison. Although the actuation strain of electrochemical actuators prepared from various electrodes did not exceed 2%, the EOP actuator easily surpassed this limiting value despite its low power consumption (specifically 23% actuation strain under 40 mW cm⁻²) (Figure Sa and Figure S24). Additionally, the high ρ_E of 1.06×10^5 J m⁻³ measured for the EOP actuator outperforms those of electrochemical actuators (<1.2 × 10⁴ J m⁻³),^{6,8} various stimuli-responsive hydrogels (<10⁴ J m⁻³),¹⁶ and mammalian skeletal muscle (<8.1 × 10³ J m⁻³)⁴⁰ reported to date (Figure Sb).

EOP actuators with various geometries were also fabricated to evaluate their potential for broad applicability. It should be noted that the morphing and actuation of the planar, curved-planar, and square-pillared structures exceeded the limit of the typical bending motion shown by previously reported electrochemical actuators. To minimize the size of external support for facile application, Au- or Pt-coated PET supports were used

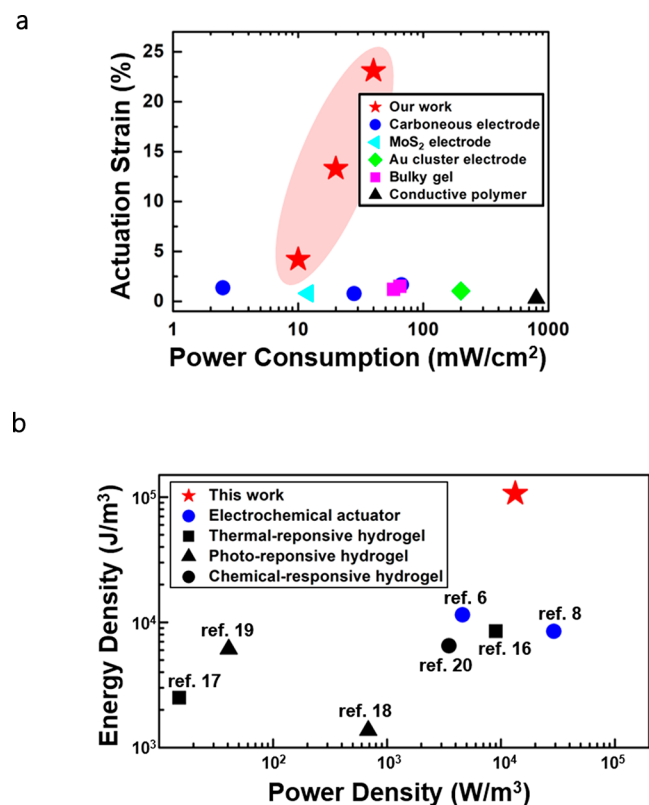


Figure 5. (a) Plots of actuation strain versus power consumption of EOP actuator and other types of electrochemical actuators. (b) Plots of energy density versus power density of EOP actuator, previously reported electrochemical actuators and other stimuli-responsive hydrogel actuators.

(Figure S17c). The planar-structured EOP actuator with thickness of 500 μm exhibited stable and efficient operation as a soft gripper (Figure 6a and Movie S5). A soft flower with an undefined and complex shape was grasped by the EOP actuator by applying a forward bias (+3 V), lifted in slow-relaxation state (0 V), and then removed by applying a reverse bias (−3 V). Additionally, our soft gripper with a weight of 32 mg and a gripping arm length of 10 mm could grasp and lift the object (battery, 1 g) which was approximately 31 times heavier than the gripper. Considering that the previously reported electrochemical actuator-based grippers can grasp and lift 153 mg of object (i.e., about 1.9 times of gripper weight),⁸ our results evidently demonstrate the excellent actuation performance of EOP actuators, which also redeem the critical drawbacks (i.e., the requirement of long gripping arms, the limited gripping range, and the low gripping force) of previously reported grippers. Furthermore, high actuation performances (i.e., slow-relaxation property, lower power consumption, and strong gripping force) shown in EOP actuators and/or EOP-based grippers imply that the energy consumption of EOP actuators is much less than those of the reported electrochemical actuators.

The curved actuator (1000 μm thick) analogous to the structural configuration of the Venus flytrap also exhibited flytraplike actuation and morphing (Figure 6b and Movie S6). Although the speed of the curved actuator was slower than that of snap-through motion by the Venus flytrap, its angular velocity could be accelerated to 64.2° s^{-1} , which followed the fundamental principle of the Venus flytrap using the accumulated elastic energy in bistable structure (Figure S25).

Moreover, it was the facile demonstration of complicated one-body electroactive morphing without any additional fabrication process. Finally, 2-DOF (i.e., two degrees of freedom) movement was accomplished by the EOP actuator with a square-pillared structure. Four sides of the EOP actuator electrode were completely separated using UV-laser cutting (Figure S26). Generally, it should be noted that conventional bulk metal- or carbon-composite-based electrodes are bendable along only one axis (i.e., the out-of-plane direction) owing to their unfavorable mechanical properties. However, in the case of our EOP actuators, their bending direction can be freely controlled according to the direction of the electric field (Figure 6c and Movie S7) because they have mechanically compliant and stress-relievable electrodes (i.e., crack electrodes) (see Figure 3). To our knowledge, the 2-DOF control of whole-body electrochemical actuators shown in this study has not been reported to date. It should also be noted that our approach can be easily applied to the hydrogel substrates with various shapes, such as micropatterned, accordion-structured, or tube-structured hydrogels for more complicated actuating movement.

CONCLUSION

We demonstrated that EOP hydrogel actuators with high actuation performance could be prepared from the LbL assembly induced cracked electrodes formed onto hydrogel, and additionally their mechanism was fundamentally different from those of soft actuators reported to date. Interfacial LbL assembly and room-temperature sintering of metal NPs at hydrophobic/hydrophilic solvent interfaces generated the interconnected, cracked, and mechanically flexible metal electrodes onto hydrogels. In this case, electric field-induced electroosmosis pumping within the cracked electrode-coated hydrogel induced bulky hydraulic flow, resulting in a whole-body actuation performance on a massive scale. The resultant actuator exhibited high actuation strain (>20%), energy density ($\sim 1.06 \times 10^5 \text{ J m}^{-3}$), and extremely low power consumption/strain (4 $\text{mW cm}^{-2} \%^{-1}$), allowing various geometries and motion with 2-DOF. In particular, given that a variety of shape- and size-controlled soft electrodes requiring high electrical conductivity and mechanical flexibility/stability cannot be easily realized by conventional physical adsorption approaches or sputtering process, our approach can provide an important basis for developing and designing a wide variety of high-performance soft electronics including soft actuators.

EXPERIMENTAL SECTION

Synthesis of Tetraoctylammonium-Stabilized Au NPs. TOA-stabilized Au NPs were synthesized by using the Brust method. Thirty millimolar gold(III) chloride trihydrate ($\text{HAuCl}_4 \cdot 3\text{H}_2\text{O}$, $\geq 99.9\%$, Sigma-Aldrich) dissolved in deionized water (30 mL) and 20 mM TOABr (98%, Sigma-Aldrich) dissolved in toluene (80 mL) were mixed by stirring for more than 30 min. The toluene phase containing the transferred metal salt was separated from the aqueous solution, and then 0.4 M aqueous solution of NaBH_4 (25 mL, 99.99%, Sigma-Aldrich) was added to the mixture. After 3 h of reaction, the toluene phase was separated again from the aqueous solution and washed with H_2SO_4 (0.1 M, 95% purity, Daejung Chemicals), NaOH (0.1 M, 97%, Sigma-Aldrich), and DI water several times.

Preparation of PAA Hydrogel Film. Acrylic acid (6.85 mL, Sigma-Aldrich) and ethylene glycol dimethacrylate (200 μL , 98%, Sigma-Aldrich) were dissolved in 6.5 mL of deionized (DI) water. Then 0.15 wt % of 2,2-dimethoxy-2-phenylacetophenone (200 μL , 99%, Sigma-Aldrich) dissolved in dimethyl sulfoxide (99.9%, Sigma-Aldrich) solution (300 μL), which was used as an initiating agent for

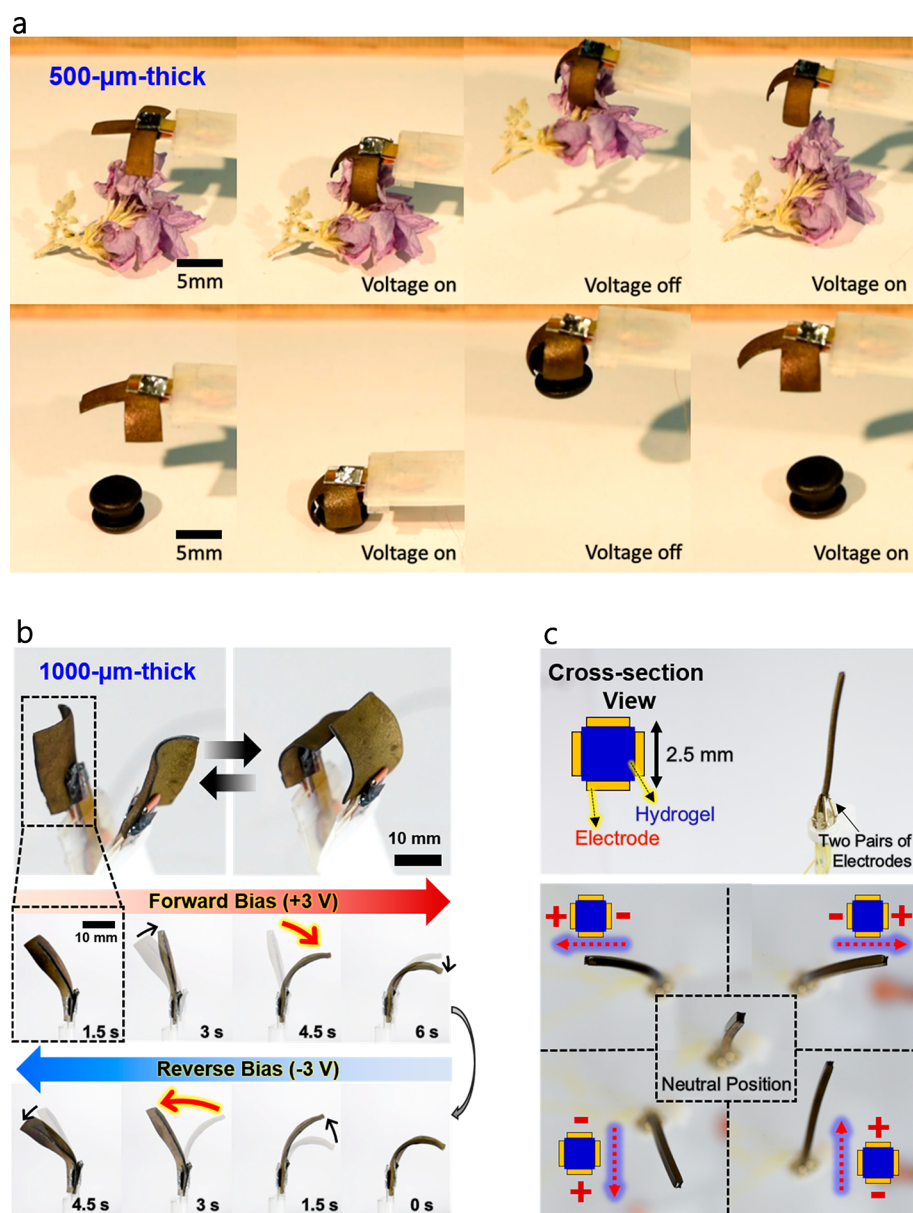


Figure 6. (a) Planar-structured soft gripper (500 μm thick) with slow-relaxation property. Objects shown in top and bottom panels show 20 mg of flower and 1000 mg of battery, respectively. (b) Bistable curved-planar-structured EOP actuator (1000 μm thick) showing flytrap-like actuation with spring-out mode. (c) One-body square-pillared-structured EOP actuator with 2-DOF actuation.

polymerization, was added to the aqueous solution. The polymerizing solution was injected into the PET mold frames with defined thicknesses (50–1000 μm) sandwiched between slide glasses. The mold-confined solutions were polymerized by irradiation of UV light (30 W) for 30 min. The resultant hydrogel films were immersed in DI water for 3 days to eliminate unreacted residuals.

Preparation of PAA-co-PAN Hydrogel Film. Acrylic acid (5.48 mL, Sigma-Aldrich), acrylonitrile (1.30 mL, Sigma-Aldrich), and ethylene glycol dimethacrylate (200 μL , 98%, Sigma-Aldrich) were dissolved in 6.5 mL of DI water. All subsequent preparation steps were identical with those used to prepare for PAA hydrogel films.

Preparation of PAA–PVA Hydrogel Film. Poly(vinyl alcohol) (0.65 g, $M_w \sim 31\,000$ –50 000, Sigma-Aldrich), glutaldehyde solution (81.2 μL 50% in DI water, Sigma-Aldrich), acrylic acid (6.85 mL, Sigma-Aldrich), and ethylene glycol dimethacrylate (200 μL , 98%, Sigma-Aldrich) were dissolved in 6.5 mL of DI water. All subsequent preparation steps were identical with those used to prepare for PAA hydrogel films.

Preparation of Electrodes on Hydrogels. Cracked electrodes with an interconnection composed of TOA-Au NPs and TREN were formed on PAA-based hydrogels. For the preparation of these electrodes, the hydrogel films were first immersed in aqueous TREN of pH 11 (5 mg mL^{-1} , $\geq 99.5\%$, Sigma-Aldrich) solution for 1 day, and then washed with DI water. In this case, the hydrogel films were fully swollen due to diffusion of TREN into/onto hydrogel films. After TREN deposition, the swollen hydrogel films were sequentially dried with mild air stream. The TREN-coated films were dipped in TOA-Au NP toluene (5 mg mL^{-1}) solution for 2 h again and then washed in toluene solvent for removing weakly adsorbed TOA-Au NPs, followed by air drying. During this deposition process, the TOA-Au NPs onto hydrogel films were converted to Au nanoplates with a thickness of approximately 115 nm, experiencing the interfacial assembly between TOA-Au NPs and TRENs (onto hydrogel) and the successive room-temperature metallic sintering of TOA-Au NPs. These processes were repeated until the desired bilayer number n of $[\text{Au NP}]_n$ onto hydrogel films (i.e., $[\text{Au NP}]_n$ -hydrogels).

Characterization of TOA-Au NPs and [Au NP]_n-Coated Hydrogels. The size of TOA-Au NPs synthesized in toluene was investigated by high-resolution transmission electron microscopy (HR-TEM, Tecnai20). Ligand exchange reaction between TOA ligands bound to the surface of Au NPs and TREN linkers were examined by Fourier transform infrared (FTIR) spectra. For qualitative investigation, TOA-Au NP and TREN were LbL-assembled onto Si wafer instead of hydrogel substrates. In this case, with increasing layer number the FTIR spectra of (TOA-Au NP/TREN)_n multilayers were measured using CARY 600 spectrometer (Agilent Technology) in specular mode with a resolution of 4 cm⁻¹. The obtained data were plotted using spectrum analysis software (OMNIC, Nicolet). For the investigation of the thickness and morphology of the (TOA-Au NP/TREN)_n multilayers (i.e., [Au NP]_n) onto hydrogel films, the cryo FE-SEM was conducted using Quanta-3D FEG (FEI). Top-view and cross-sectional images were obtained at -180 °C. The sheet resistance was measured using four-point probe (MCP-T610, Mitsubishi Chemical Analytech) and two-point probe (Keithley 4200-SCS).

Molecular Dynamics Simulations. All-atom molecular dynamics (MD) simulations were performed for a model system consisting of two TOA-Au NPs (diameter ~3.5 nm) dispersed in toluene interfaced with water containing TRENS. To build the initial molecular configuration of two separate layers (TOA-Au NPs in toluene and TREN in water) interfaced with each other, isothermal–isobaric MD simulations were performed separately for each layer with appropriately chosen molecular composition (for the consideration of merging layers that should share the same area of plane for the interface) at 298 K and 1 bar, followed by the merging of two layers independently equilibrated by MD runs. With this initial configuration, isothermal–isobaric MD simulations were carried out at 298 K and 1 bar using Forcite module with COMPASS (condensed-phase optimized molecular potentials for atomistic simulation studies) force field⁵¹ (COMPASS II) as implemented in Material Studio package, a well-known general force field for all-atom scale simulations of a wide variety of molecular systems ranging from common organic and inorganic small molecules to polymers. The Nose–Hoover–Langevin thermostat⁵² and Berendsen barostat⁵³ were used to maintain temperature (298 K) and pressure (1 bar). It is worth pointing out that the fluctuations of the simulation box in *Movie S1* are unnoticeably small, which is partly due to low diffusive Au particles and mainly due to isotropic barostat (Berendsen barostat) employed in the present simulation. Additionally, when MD simulation was done at the isothermal–isobaric ensemble (NPT ensemble), the volume change recorded during the simulation time was negligible (*Figure S27*), which was mainly attributed to heavy and very-low diffusive Au particles that have an extremely large resistance to volume change.

Preparation of Actuator Operation. Four edges of [Au NP]₅-coated hydrogels were cut to achieve electrical separation between the top and bottom sides of samples. In the case of square-pillared samples, the four sides of the electrode were completely separated using UV-laser cutting along the edges. After laser cutting, the samples were dipped in the 1:1 mixture of aqueous TREN solution and 1-ethyl-3-methylimidazolium tetrafluoroborate ([EMIM][BF₄]) for the infiltration of hydrated ionic fluid into hydrogels.

Measurement of Actuator Performance. The samples (i.e., [Au NP]₅-coated hydrogels) were placed in contact with platinum-coated poles (2 mm diameter) to connect them to external power sources at the 20 °C and humidity of 40%. After applying voltages, the bending of actuators was recorded by a digital camera (Cannon EOS 301) at 30 frames per second. The actuation strain was calculated by using the bending radius and thickness of the actuators based on previously defined relationships^{54,55}

$$\varepsilon = \frac{\Delta L_1 + \Delta L_2}{L} = \frac{d}{R}$$

$$\left(\frac{R - \frac{d}{2}}{R + \frac{d}{2}} = \frac{L + \Delta L_2}{L + \Delta L_1} \right)$$

where ε is the actuation strain, L is the length of the actuator, ΔL_1 is the length change of outermost part of the actuator, ΔL_2 is the length change of the innermost part of the actuator, d is the thickness of the actuator, and R is the bending radius of the actuator. For elastically actuated materials, the ρ_E and ρ_W of the actuator was approximated as

$$\rho_E = \frac{E\Delta\varepsilon^2}{2}$$

$$\rho_W = \frac{\rho_E}{t}$$

where E , ε , t , ρ_E , and ρ_W are Young's modulus of the actuator, actuation strain of the actuator, time taken for one cycle, energy density (by unit-volume basis), and power density (by unit-volume basis).

ASSOCIATED CONTENT

Supporting Information

The Supporting Information is available free of charge at <https://pubs.acs.org/doi/10.1021/acsnano.0c04899>.

Schemes of typical electroosmosis device and our electroosmotic pump-driven actuator, illustration of interconnected cracked electrodes, HR-TEM images of TOA-Au NPs, FE-SEM images of room-temperature-sintered Au NPs, photographic and FE-SEM images of TREN/TOA-Au NP multilayers, photographic images of EOP actuators, tensile stress–strain curves of TREN/TOA-Au NP multilayers, FE-SEM image of hydrogel, sheet resistance and resistance changes of TREN/TOA-Au NP multilayer-coated hydrogels, FE-SEM image of TREN/TOA-Au NP multilayer-coated hydrogels after bending test and actuation, current density measured from TREN/TOA-Au NP multilayer-coated hydrogels, illustration and photographic image of EOP actuator, time-dependent actuation strain and time-dependent bending strain of EOP actuators, actuation stability and maximum blocking forces of EOP actuator, actuation strain-power consumption dependency of previously reported electrochemical actuators, time-dependent bending angle and angle velocity of EOP actuator, schematic illustration of square-pillared EOP actuator, and NPT simulation (PDF)

(*Movie S1*) MD Simulation of AuNP sintering; (*Movie S2*) Electroosmosis pumping by interconnected cracked electrode on PAA-co-PAN hydrogel; (*Movie S3*) Actuation of EOP actuator with different thickness; (*Movie S4*) Demonstration of spring-out mode; (*Movie S5*) Soft gripper by planar structure; (*Movie S6*) Flytrap-like actuation by curved-planar structure; (*Movie S7*) 2-DOF actuation by square-pillared structure (ZIP)

AUTHOR INFORMATION

Corresponding Authors

Jinhan Cho – Department of Chemical and Biological Engineering, Korea University, Seoul 02841, Republic of Korea; orcid.org/0000-0002-7097-5968; Email: jinhan71@korea.ac.kr

Je-Sung Koh – Department of Mechanical Engineering, Ajou University, Suwon 16499, Republic of Korea; Email: jskoh@ajou.ac.kr

Authors

Jongkuk Ko – Department of Chemical and Biological Engineering, Korea University, Seoul 02841, Republic of Korea; orcid.org/0000-0002-8278-6718

Dongjin Kim – Department of Mechanical Engineering, Ajou University, Suwon 16499, Republic of Korea

Yongkwon Song – Department of Chemical and Biological Engineering, Korea University, Seoul 02841, Republic of Korea;
orcid.org/0000-0002-2173-8157

Seokmin Lee – Department of Chemical and Biological Engineering, Korea University, Seoul 02841, Republic of Korea;
orcid.org/0000-0001-6616-0064

Minseong Kwon – Department of Chemical and Biological Engineering, Korea University, Seoul 02841, Republic of Korea;
orcid.org/0000-0001-6313-6237

Seungyong Han – Department of Mechanical Engineering, Ajou University, Suwon 16499, Republic of Korea

Daeshik Kang – Department of Mechanical Engineering, Ajou University, Suwon 16499, Republic of Korea

Yongju Kim – KU-KIST Graduate School of Converging Science and Technology, Korea University, Seoul 02841, Republic of Korea

June Huh – Department of Chemical and Biological Engineering, Korea University, Seoul 02841, Republic of Korea

Complete contact information is available at:
<https://pubs.acs.org/10.1021/acsnano.0c04899>

Author Contributions

The manuscript was written by J.K., J.H., and J.C. The experimental results and details were discussed by J.K., D.K., J.H., J.K., and J.C. The results were also checked and reviewed through contributions of all authors. All authors have given approval to the final version of the manuscript.

Notes

The authors declare no competing financial interest.

ACKNOWLEDGMENTS

This work was supported by a National Research Foundation (NRF) funded by the Ministry of Education of Korea (2019R1A4A1027627; 2018R1A2A1A05019452; 2019R1F1A1063066) and the new faculty research fund of Ajou University and the Ajou University research fund.

REFERENCES

- (1) Osada, Y.; Okuzaki, H.; Hori, H. A Polymer Gel with Electrically Driven Motility. *Nature* **1992**, *355*, 242–244.
- (2) Lu, W.; Fadeev, A. G.; Qi, B.; Smela, E.; Mattes, B. R.; Ding, J.; Spinks, G. M.; Mazurkiewicz, J.; Zhou, D.; Wallace, G. G.; MacFarlane, D. R.; Forsyth, S. A.; Forsyth, M. Use of Ionic Liquids for π -Conjugated Polymer Electrochemical Devices. *Science* **2002**, *297*, 983–987.
- (3) Kim, O.; Kim, H.; Choi, U. H.; Park, M. J. One-Volt-Driven Superfast Polymer Actuators Based on Single-Ion Conductors. *Nat. Commun.* **2016**, *7*, 13576.
- (4) Yan, Y.; Santaniello, T.; Bettini, L. G.; Minnai, C.; Bellacicca, A.; Porotti, R.; Denti, I.; Faraone, G.; Merlini, M.; Lenardi, C.; Milani, P. Electroactive Ionic Soft Actuators with Monolithically Integrated Gold Nanocomposite Electrodes. *Adv. Mater.* **2017**, *29*, 1606109.
- (5) Acerce, M.; Akdoğan, E. K.; Chhowalla, M. Metallic Molybdenum Disulfide Nanosheet-Based Electrochemical Actuators. *Nature* **2017**, *549*, 370–373.
- (6) Lu, C.; Yang, Y.; Wang, J.; Fu, R.; Zhao, X.; Zhao, L.; Ming, Y.; Hu, Y.; Lin, H.; Tao, X.; Li, Y.; Chen, W. High-Performance Graphdiyne-Based Electrochemical Actuators. *Nat. Commun.* **2018**, *9*, 752.
- (7) Umrao, S.; Tabassian, R.; Kim, J.; Nguyen, V. H.; Zhou, Q.; Nam, S.; Oh, I.-K. MXene Artificial Muscles Based on Ionically Cross-Linked $Ti_3C_2T_x$ Electrode for Kinetic Soft Robotics. *Sci. Robot.* **2019**, *4*, No. eaaw7797.

(8) Wu, G.; Wu, X.; Xu, Y.; Cheng, H.; Meng, J.; Yu, Q.; Shi, X.; Zhang, K.; Chen, W.; Chen, S. High-Performance Hierarchical Black-Phosphorous-Based Soft Electrochemical Actuators in Bioinspired Applications. *Adv. Mater.* **2019**, *31*, No. 1806492.

(9) Wang, H. S.; Cho, J.; Song, D. S.; Jang, H. H.; Jho, J. Y.; Park, J. H. High-Performance Electroactive Polymer Actuators Based on Ultrathick Ionic Polymer–Metal Composites with Nanodispersed Metal Electrodes. *ACS Appl. Mater. Interfaces* **2017**, *9*, 21998–22005.

(10) Lu, L.; Liu, J.; Hu, Y.; Zhang, Y.; Randriamahazaka, H.; Chen, W. Highly Stable Air Working Bimorph Actuator Based on a Graphene Nanosheet/Carbon Nanotube Hybrid Electrode. *Adv. Mater.* **2012**, *24*, 4317–4321.

(11) Kotal, M.; Kim, J.; Kim, K. J.; Oh, I.-K. Sulfur and Nitrogen Co-Doped Graphene Electrodes for High-Performance Ionic Artificial Muscles. *Adv. Mater.* **2016**, *28*, 1610–1615.

(12) Kotal, M.; Kim, J.; Tabassian, R.; Roy, S.; Nguyen, V. H.; Koratkar, N.; Oh, I.-K. Highly Bendable Ionic Soft Actuator Based on Nitrogen-Enriched 3D Hetero-Nanostructure Electrode. *Adv. Funct. Mater.* **2018**, *28*, 1802464.

(13) Shahinpoor, M.; Kim, K. J. The Effect of Surface-Electrode Resistance on the Performance of Ionic Polymer–Metal Composite (IPMC) Artificial Muscles. *Smart Mater. Struct.* **2000**, *9*, 543.

(14) Nemat-Nasser, S.; Thomas, C. W. *Ionometric Polymer–Metal Composites. Electroactive Polymer (EAP) Actuators as Artificial Muscles—Reality, Potential, and Challenges*, 2nd ed.; SPIE: Bellingham, WA, 2004.

(15) Oh, C.; Kim, S.; Kim, H.; Park, G.; Kim, J.; Ryu, J.; Li, P.; Lee, S.; No, K.; Hong, S. Effects of Membrane Thickness on the Performance of Ionic Polymer–Metal Composite Actuators. *RSC Adv.* **2019**, *9*, 14621–14626.

(16) Kim, J.; Hanna, J. A.; Byun, M.; Santangelo, C. D.; Hayward, R. C. Designing Responsive Buckled Surfaces by Half-tone Gel Lithography. *Science* **2012**, *335*, 1201–1205.

(17) Gladman, A. S.; Matsumoto, E. A.; Nuzzo, R. G.; Mahadevan, L.; Lewis, J. A. Biomimetic 4D Printing. *Nat. Mater.* **2016**, *15*, 413–418.

(18) Qian, X.; Zhao, Y.; Alsaied, Y.; Wang, Xu.; Hua, M.; Galy, T.; Gopalakrishna, H.; Yang, Y.; Cui, J.; Liu, N.; Marszewski, M.; Pilon, L.; Jiang, H.; He, X. Artificial Phototropism for Omnidirectional Tracking and Harvesting of Light. *Nat. Nanotechnol.* **2019**, *14*, 1048–1055.

(19) Li, G.; Gao, T.; Fan, G.; Liu, Z.; Liu, Z.; Jiang, J.; Zhao, Y. Photoresponsive Shape Memory Hydrogels for Complex Deformation and Solvent-Driven Actuation. *ACS Appl. Mater. Interfaces* **2020**, *12*, 6407–6418.

(20) Huang, L.; Jiang, R.; Wu, J.; Song, J.; Bai, H.; Li, B.; Zhao, Q.; Xie, T. Ultrafast Digital Printing toward 4D Shape Changing Materials. *Adv. Mater.* **2017**, *29*, 1605390.

(21) Cangialosi, A.; Yoon, C. K.; Liu, J.; Huang, Q.; Guo, J.; Nguyen, T. D.; Gracias, D. H.; Schulman, R. DNA Sequence-Directed Shape Change of Photopatterned Hydrogels via High-Degree Swelling. *Science* **2017**, *357*, 1126–1130.

(22) Ma, C.; Le, X.; Tang, X.; He, J.; Xiao, P.; Zheng, J.; Xiao, H.; Lu, W.; Zhang, J.; Huang, Y.; Chen, T. A Multiresponsive Anisotropic Hydrogel with Macroscopic 3D Complex Deformations. *Adv. Funct. Mater.* **2016**, *26*, 8670–8676.

(23) Ma, Y.; Zhang, Y.; Wu, B.; Sun, W.; Li, Z.; Sun, J. Polyelectrolyte Multilayer Films for Building Energetic Walking Device. *Angew. Chem., Int. Ed.* **2011**, *50*, 6254–6257.

(24) Ji, M.; Jiang, N.; Chang, J.; Sun, J. Near-Infrared Light-Driven, Highly Efficient Bilayer Actuators Based on Polydopamine-Modified Reduced Graphene Oxide. *Adv. Funct. Mater.* **2014**, *24*, 5412–5419.

(25) Lunni, D.; Cianchetti, M.; Filippeschi, C.; Sinibaldi, E.; Mazzolai, B. Plant-Inspired Soft Bistable Structures Based on Hygroscopic Electrospun Nanofibers. *Adv. Mater. Interfaces* **2020**, *7*, 1901310.

(26) Stuetzer, O. M. Ion Drag Pumps. *J. Appl. Phys.* **1960**, *31*, 136–146.

(27) Iverson, B. D.; Garimella, S. V. Recent Advances in Microscale Pumping Technologies: A Review and Evaluation. *Microfluid. Nanofluid.* **2008**, *5*, 145–174.

(28) Snyder, J. L.; Getpreechawsawas, J.; Fang, D. Z.; Gaboriski, T. R.; Striemer, C. C.; Fauchet, P. M.; Borkholder, D. A.; McGrath, J. L. High-

Performance, Low-Voltage Electroosmotic Pumps with Molecularly Thin Silicon Nanomembrane. *Proc. Natl. Acad. Sci. U. S. A.* **2013**, *110*, 18425–18430.

(29) Wu, X.; Rajasekaran, P. R.; Martin, C. R. An Alternating Current Electroosmotic Pump Based on Conical Nanopore Membranes. *ACS Nano* **2016**, *10*, 4637–4643.

(30) Hossain, M. R.; Dutta, D.; Islam, N.; Dutta, P. Review: Electric Field Driven Pumping in Microfluidic Device. *Electrophoresis* **2018**, *39*, 702–731.

(31) Cacucciolo, V.; Shintake, J.; Kuwajima, Y.; Maeda, S.; Floreano, D.; Shea, H. Stretchable Pumps for Soft Machines. *Nature* **2019**, *572*, 516–519.

(32) Must, I.; Sinibaldi, E.; Mazzolai, B. A Variable-Stiffness Tentacle-Like Soft Robot Based on Reversible Osmotic Actuation. *Nat. Commun.* **2019**, *10*, 344.

(33) Sinibaldi, E.; Puleo, G. L.; Mattioli, F.; Mattoli, V.; Di Michele, F.; Beccai, L.; Tramacere, F.; Mancuso, S.; Mazzolai, B. Osmotic Actuation Modelling for Innovative Biorobotic Solutions Inspired by the Plant Kingdom. *Bioinspiration Biomimetics* **2013**, *8*, 025002.

(34) Sinibaldi, E.; Argiolas, A.; Puleo, G. L.; Mazzolai, B. Another Lesson from Plants: The Forward Osmosis-Based Actuator. *PLoS One* **2014**, *9*, No. e102461.

(35) Arens, L.; Weisfenfeld, F.; Klein, C. O.; Schlag, K.; Wilhelm, M. Osmotic Engine: Translating Osmotic Pressure into Macroscopic Mechanical Force via Poly(acrylic Acid) Based Hydrogels. *Adv. Sci.* **2017**, *4*, 1700112.

(36) Kang, D.; Pikhitsa, P. V.; Choi, Y. W.; Lee, C.; Shin, S. S.; Piao, L.; Park, B.; Suh, K.-Y.; Kim, T.; Choi, M. Ultrasensitive Mechanical Crack-Based Sensor Inspired by the Spider Sensory System. *Nature* **2014**, *516*, 222–226.

(37) Kim, S.; Jang, S.; Kim, S. M.; Ahn, C.-Y.; Hwang, W.; Cho, Y.-H.; Sung, Y.-E.; Choi, M. Reduction of Methanol Crossover by Thin Cracked Metal Barriers at the Interface between Membrane and Electrode in Direct Methanol Fuel Cells. *J. Power Sources* **2017**, *363*, 153–160.

(38) Lee, J.; Kim, S.; Lee, J.; Yang, D.; Park, B. C.; Ryu, S.; Park, I. A Stretchable Strain Sensor Based on a Metal Nanoparticle Thin Film for Human Motion Detection. *Nanoscale* **2014**, *6*, 11932–11939.

(39) Jun, K.; Kim, J.; Oh, I.-K. An Electroactive and Transparent Haptic Interface Utilizing Soft Elastomer Actuators with Silver Nanowire Electrodes. *Small* **2018**, *14*, 1801603.

(40) Mirfakhrai, T.; Madden, J. D. W.; Baughman, R. H. Polymer Artificial Muscles. *Mater. Today* **2007**, *10*, 30–38.

(41) Udayabhaskararao, T.; Altantzis, T.; Houben, L.; Coronado-Puchau, M.; Langer, J.; Popovitz-Biro, R.; Liz-Marzán, L. M.; Vuković, L.; Král, P.; Bals, S.; Klajn, R. Tunable Porous Nanoalloys Prepared by Post-Assembly Etching of Binary Nanoparticle Superlattices. *Science* **2017**, *358*, 514–518.

(42) Schmitt, J.; Decher, G.; Dressick, W. J.; Brandow, S. L.; Geer, R. E.; Shashidhar, R.; Calvert, J. M. Metal Nanoparticle/Polymer Superlattice Films: Fabrication and Control of Layer Structure. *Adv. Mater.* **1997**, *9*, 61–65.

(43) Caruso, F.; Caruso, R. A.; Möhwald, H. Nanoengineering of Inorganic and Hybrid Hollow Spheres by Colloidal Templating. *Science* **1998**, *282*, 1111–1114.

(44) Kim, Y.; Zhu, J.; Yeom, B.; Di Prima, M.; Su, X.; Kim, J.-G.; Yoo, S. J.; Uher, C.; Kotov, N. A. Stretchable Nanoparticle Conductors with Self-Organized Conductive Pathways. *Nature* **2013**, *500*, 59–63.

(45) Ko, Y.; Kwon, M.; Bae, W. K.; Lee, B.; Lee, S. W.; Cho, J. Flexible Supercapacitor Electrodes Based on Real Metal-Like Cellulose Papers. *Nat. Commun.* **2017**, *8*, 536.

(46) Ma, S.; Zhang, Y.; Liang, Y.; Ren, L.; Tian, W.; Ren, L. High-Performance Ionic-Polymer–Metal Composite: Toward Large-Deformation Fast-Response Artificial Muscles. *Adv. Funct. Mater.* **2020**, *30*, 1908508.

(47) Kim, S. J.; Kim, O.; Park, M. J. True Low-Power Self-Locking Soft Actuators. *Adv. Mater.* **2018**, *30*, 1706547.

(48) Shahinpoor, M. Biomimetic Robotic Venus Flytrap (*Dionaea muscipula Ellis*) Made with Ionic Polymer Metal Composites. *Bioinspiration Biomimetics* **2011**, *6*, 046004.

(49) Kim, S.-W.; Koh, J.-S.; Lee, J.-G.; Ryu, J.; Cho, M.; Cho, K.-J. Flytrap-Inspired Robot Using Structurally Integrated Actuation Based on Bistability and a Developable Surface. *Bioinspiration Biomimetics* **2014**, *9*, 036004.

(50) Fan, W.; Shan, C.; Guo, H.; Sang, J.; Wang, R.; Zheng, R.; Sui, K.; Nie, Z. Dual-Gradient Enabled Ultrafast Biomimetic Snapping of Hydrogel Materials. *Sci. Adv.* **2019**, *5*, No. eaav7174.

(51) Sun, H. An *Ab Initio* Force-Field Optimized for Condensed-Phase Applications - Overview with Details on Alkane and Benzene Compounds. *J. Phys. Chem. B* **1998**, *102*, 7338–7364.

(52) Samoletov, A. A.; Dettmann, C. P.; Chaplain, M. A. J. Thermostats for "Slow" Configurational Modes. *J. Stat. Phys.* **2007**, *128*, 1321–1336.

(53) Berendsen, H. J. C.; Postma, J. P. M.; van Gunsteren, W. F.; DiNola, A.; Haak, J. R. Molecular Dynamics with Coupling to an External Bath. *J. Chem. Phys.* **1984**, *81*, 3684–3690.

(54) Pei, Q.; Inganaes, O. Electrochemical Applications of the Bending Beam Method. 1. Mass Transport and Volume Changes in Polypyrrole During Redox. *J. Phys. Chem.* **1992**, *96*, 10507–10514.

(55) Takeuchi, I.; Asaka, K.; Kiyohara, K.; Sugino, T.; Terasawa, N.; Mukai, K.; Fukushima, T.; Aida, T. Electromechanical Behavior of Fully Plastic Actuators Based on Bucky Gel Containing Various Internal Ionic Liquids. *Electrochim. Acta* **2009**, *54*, 1762–1768.